Check for updates

# Fluorinated organosilane polycondensation enables a robust Si anode for lithium storage†

Zhengyue Li,[a] Jiecheng Huang[a] and Zhiyu Wang ⓘ *[ab]

**The chemistry of fluorinated organosilane polycondensation is utilized to form a robust Si anode with F-doped $SiO_x$/C composite coating. F-doping promotes the formation of not only a coating rich in less electrochemically active $Si^{4+}$ species but also an LiF-rich solid-state electrolyte interphase, enabling an Si anode with a long life of 500 cycles at large current densities for lithium storage.**

Si has been recognized as the next-generation anode material for advancing lithium-ion batteries due to its exceptional capacity and abundant availability.[1–4] However, Si anodes generally experience drastic volume expansion ($>400\%$) upon lithiation, inducing severe electrode pulverization. This effect greatly shortens the lifetime of Si anodes due to active material loss and cumulative growth of the solid electrolyte interface (SEI).[5,6] To address these challenges, various strategies have been developed, such as dimensional engineering,[7,8] flexible surface coating,[9,10] binder engineering,[11,12] and electrolyte optimization.[13,14] Specifically, encapsulating Si within a thick carbon coating is demonstrated to be effective and industrially viable for stabilizing Si anodes while reducing side reactions of electrolyte decomposition. Nevertheless, conventional carbon coatings have limited robustness, making them insufficient for safeguarding Si anodes against long-term cycling.[15] Moreover, the SEI properties are also critical to extending the lifespan of an Si anode for lithium storage. Formation of a robust SEI is highly desired to passivate the Si anode and minimize side reactions, which is challenging to achieve with carbon coatings alone.

Herein, we propose an effective way of reinforcing the Si anode through an F-doped $SiO_x$/C composite coating strategy. This coating is designed from fluorinated organosilane polycondensation, aiming to deliver a combination of high robustness, improved conductivity, and the ability to guide Li-rich SEI formation during lithium storage. Benefiting from a synergy of

these improvements, the lifetime of the Si anode with F–$SiO_x$/C coating can be extended to 500 cycles, with high capacity retention and good rate capability.

Si nanoparticles (NPs) with F–$SiO_x$/C coating (Si@F–$SiO_x$/C-1) are prepared by hydrolysis–polycondensation of organosilane, followed by annealing (Fig. 1). First, vinyltri(2-methoxyethoxy)-silane (VTES) and F-containing trimethoxy(3,3,3-trifluoropropyl)-silane (TFPS) are subjected to acidic hydrolysis in the presence of Si NPs (step I). In this process, the ethoxy group on VTES and the methoxy group on TFPS are hydrolyzed into hydroxyl groups. They subsequently interact with each other and with the silanol groups on the Si surface (step II). This chemical bridging facilitates the formation of a robust and dense coating of polymerized organo-silicon on Si NPs (Si@POS). Upon the next annealing, the –Si–O– bonds within polymerized organosilicon transform to $SiO_x$, while the trifluoropropyl groups in TFPS convert to F-doped amorphous carbon (step III).[16] Eventually, Si NPs with the F-doped $SiO_x$/C composite coating are obtained for lithium storage.

Si@F–$SiO_x$/C-1 comprises interconnected spherical particles of varying sizes (Fig. 2a and b). This characteristic is desirable for reducing the anode surface area and side reactions linked to electrolyte consumption. It also prevents individual Si NPs from detaching and electric isolation from the current collector. Transmission electron microscopy (TEM) shows the presence of Si NPs with a small size of 100–200 nm as the fundamental unit of Si@F–$SiO_x$/C-1 (Fig. 2c). Elemental mapping shows the uniform distribution of Si, C, O, and F elements within Si@F–$SiO_x$/C-1 (Fig. 2d). In the X-ray diffraction (XRD) pattern of Si@F–$SiO_x$/C-1, the diffraction peaks at 28°, 47°, 56°, 69°, and 76° correspond to the (111), (220), (311), (400), and (331) planes of crystalline Si, respectively (Fig. S1, ESI†). A broad peak in the range of 17–25° stems from the disordered $SiO_x$ and carbon derived from the organosilicon coating on Si NPs.[17] The Fourier transform infrared (FTIR) spectrum of Si@POS displays absorbance bands at 830, 897, 1064 and 1103, 1210, and 1263 $cm^{-1}$, ascribed to the bending vibrations of Si–O–O–Si and Si–OH bonds and the asymmetric stretching vibrations of Si–O–Si, Si–O–C and C–F bonds, respectively (Fig. 2e).[18–20] After annealing, only the bending and asymmetric stretching vibrations of Si–O–Si

[a] State Key Lab of Fine Chemicals, Liaoning Key Lab for Energy Materials and Chemical Engineering, School of Chemical Engineering, Dalian University of Technology, Dalian 116024, China. E-mail: zywang@dlut.edu.cn
[b] Branch of New Material Development, Valiant Co. Ltd., Yantai, 265503, China
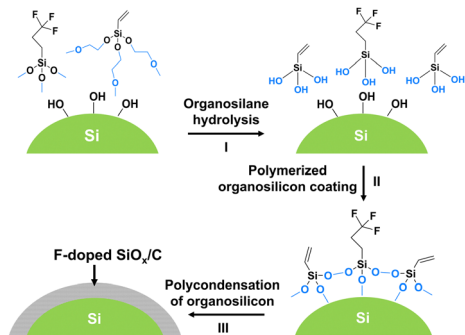
Fig. 1 Schematic illustration of the formation of Si@F−SiO$_x$/C-1 by hydrolysis−polycondensation of VTES and TFPS on Si NPs, followed by annealing.
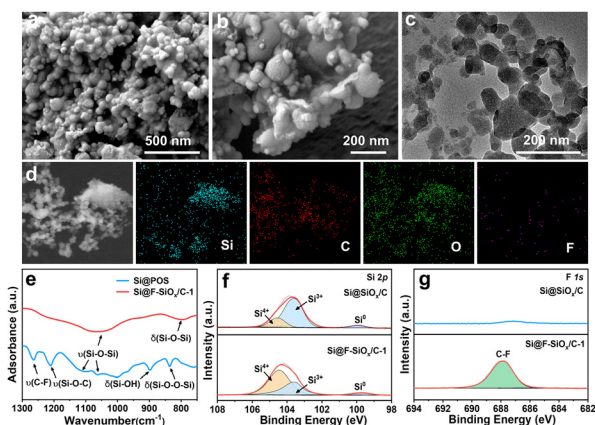


Fig. 2 (a) and (b) SEM and (c) TEM image of Si@F−SiO$_x$/C-1 consisting of interconnected NPs. (d) Elemental mapping showing the uniform dispersion of Si, C, O, and F elements within Si@F−SiO$_x$/C-1. (e) FT-IR spectra of Si@F−SiO$_x$/C-1 and Si@POS. (f) High-resolution XPS spectra for (f) Si 2p and (g) F 1s signals of Si@F−SiO$_x$/C-1 and Si@SiO$_x$/C.

bonds remain, indicating complete polycondensation of organosilicon into F-doped SiO$_x$/C by breaking C–F, Si–O–C and Si–O–O–Si bonds.

The X-ray photoelectron (XPS) spectrum reveals the coexistence of F, O, C, and Si elements in Si@F–SiO$_x$/C-1 (Fig. S2, ESI†), in contrast to Si@SiO$_x$/C containing negligible F. In the Si 2p spectrum, three peaks at 104.6, 103.6, and 99.9 eV correspond to Si$^{4+}$, Si$^{3+}$ and Si$^0$ species, respectively (Fig. 2f).[21] The presence of electronegative F facilitates the formation of an F–SiO$_x$/C coating rich in Si$^{4+}$ species, whereas electrochemically active Si$^{3+}$ is the major species in F-free Si@SiO$_x$/C. The presence of F in Si@F–SiO$_x$/C-1 is validated by the peak at 688.0 eV for the C–F bond in the F 1s spectrum (Fig. 2g).[22] The Raman spectrum of Si@F–SiO$_x$/C-1 reveals the presence of carbon by disordered (D) and graphitic (G) bands at ca. 1334 and 1603 cm$^{-1}$, respectively (Fig. S3, ESI†). The bands at ca. 506 and 1086 cm$^{-1}$ stem from crystalline Si. Si@F–SiO$_x$/C-1 has ca. 0.95 wt% F and ca. 9.4 wt% C, respectively.

Si@F–SiO$_x$/C-1 delivers an initial discharge and charge capacity of 1430 and 720 mA h g$^{-1}$ at a current density of 0.1 A g$^{-1}$ between 0.01 and 1.5 V (vs. Li/Li$^+$), respectively. The initial capacity loss of 49.6% arises from irreversible processes such as electrolyte decomposition, SEI formation,[23] and the generation

of partially electrochemical active lithium silicate as a lithiation product of SiO$_x$/C.[24] It is expected that the initial Coulombic efficiency (ICE) could be enhanced by employing electrochemical pre-lithiation or chemical pre-lithiation reagents such as Li–Naph or Li–Bp. From the second cycle onwards, Si@F–SiO$_x$/C-1 exhibits a discharge capacity of 673 mA h g$^{-1}$ and maintains high Coulombic efficiency exceeding 99.3% after 100 cycles (Fig. 3b). In contrast, bare Si NPs lose nearly all the capacities within 20–30 cycles. When cycled at higher current densities of 0.3–2.0 A g$^{-1}$, Si@F–SiO$_x$/C-1 retains high capacities of 400–670 mA h g$^{-1}$, respectively (Fig. 3c and Fig. S4, ESI†). Upon abruptly switching back the current rate to 0.1 A g$^{-1}$, a high capacity of 720 mA h g$^{-1}$ is retained, indicating robust structural stability against rapid volume change at high rates. In contrast, Si@F–SiO$_x$ without the carbon component in the coating layer suffers rapid capacity decay to 217–480 mA h g$^{-1}$ at current densities of 0.3–1.0 A g$^{-1}$, leaving negligible capacities at 2.0 A g$^{-1}$. However, the capacity can be largely restored upon reverting to 0.1 A g$^{-1}$, suggesting that the performance decay of this anode at high rates primarily results from sluggish conductivity of the F–SiO$_x$ coating rather than structural damage of Si NPs. This observation underscores the crucial role of conductive carbon within the F–SiO$_x$/C coating in improving the rate capability of Si@F–SiO$_x$/C-1. It can be further validated by a lower charge-transfer impedance ($R_{ct}$) of Si@F–SiO$_x$/C-1 relative to Si@F–SiO$_x$ without involving carbon (Fig. S5, ESI†). Moreover, the reduced SEI impedance ($R_{SEI}$) of Si@F–SiO$_x$/C-1 (8.43 Ω) compared to that of Si@SiO$_x$/C (25.3 Ω) and Si@F–SiO$_x$ (28.67 Ω) suggests the importance of F-doping in enhancing ionic conductivity of the SEI around Si@F–SiO$_x$/C-1.

When cycled at 0.3 A g$^{-1}$, Si@F–SiO$_x$/C-1 delivers a high capacity of 570 mA h g$^{-1}$ after 300 cycles with a stable capacity retention of 83.8% (Fig. 3d). A lack of flexible and conductive carbon components in the SiO$_x$ coating makes it insufficient for maintaining the long-term cycling stability of Si NPs, despite its effectiveness over short periods. Therefore, Si@F–SiO$_x$ suffers rapid capacity decay after 170 cycles, leaving a low capacity of 300 mA h g$^{-1}$ after 300 cycles. For F-free Si@SiO$_x$/C, it delivers higher capacities than Si@F–SiO$_x$/C-1 due to the dominance of electrochemically active Si$^{3+}$ species in the SiO$_x$/C coating. However, this anode suffers fast capacity fading after 110 cycles to exhibit a low capacity of 299 mA h g$^{-1}$ after 300 cycles. It suggests that while the presence of excessive Si$^{3+}$ may offer extra capacities, it compromises the coating stability and cycling performance of the Si anode after a long period. When cycled at a large current density of 1 A g$^{-1}$, Si@F–SiO$_x$/C-1 shows a long life of 500 cycles with an ICE of 42.4%, with a high capacity retention of 87.5%. This translates to a slow capacity loss of 0.025% per cycle, underscoring its excellent long-term durability (Fig. 3e). Compared to the reported Si anode, the Si@F–SiO$_x$/C-1 anode exhibits comparable capacities, while surpassing them in cycle life (Table S1, ESI†).

The lithium storage behavior of Si@F–SiO$_x$/C-1 is studied by cyclic voltammetry (CV) between 0.01 and 1.5 V (vs. Li/Li$^+$) at a scan rate of 0.2 mV s$^{-1}$. In the first cycle, a broad reduction peak appears at 0.15–0.6 V (vs. Li/Li$^+$) due to irreversible processes such as SEI formation and electrolyte decomposition.[25] A weaker reduction peak at ca. 1.2 V (vs. Li/Li$^+$) is due to the transformation of SiO$_x$ in the F–SiO$_x$/C coating into lithium silicate and lithium oxide (Fig. S6a,
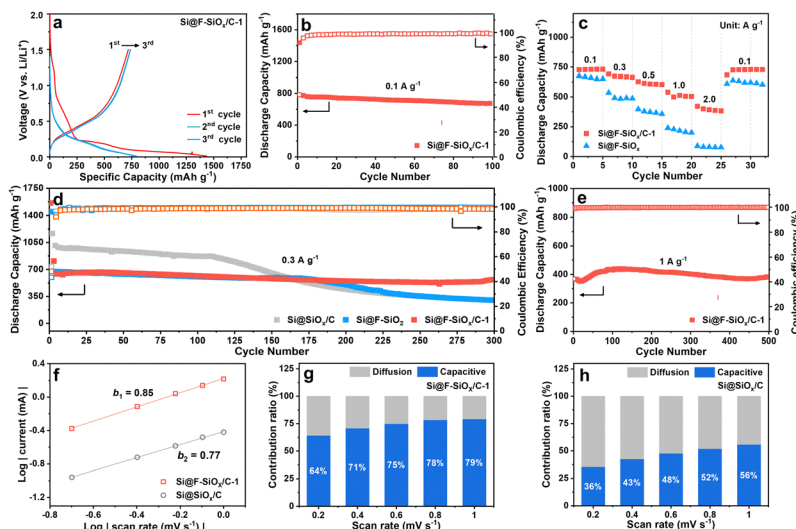
**Fig. 3** (a) Discharge–charge curves and (b) cycling stability of Si@F–SiO$_x$/C-1 at 0.1 A g$^{-1}$ between 0.01 and 1.5 V (*vs.* Li/Li$^+$). (c) Rate capability of Si@F–SiO$_x$/C and Si@F–SiO$_x$ at various current densities. (d) Cycling performance of Si@F–SiO$_x$/C-1, Si@F–SiO$_x$, and Si@SiO$_x$/C at 0.3 A g$^{-1}$. (e) Long-term stability of Si@F–SiO$_x$/C-1 at 1.0 A g$^{-1}$. (f) Relationship between scan rate and peak current for Si@F–SiO$_x$/C-1 and Si@SiO$_x$/C. The contribution ratios of diffusion-controlled and capacitance processes for lithium storage in (g) Si@F–SiO$_x$/C-1 and (h) Si@SiO$_x$/C at various scan rates.

ESI†). These irreversible reactions induce initial irreversible capacity loss of Si@F–SiO$_x$/C-1. The reduction peak below *ca.* 0.05–0.1 V (*vs.* Li/Li$^+$) relates to Si alloying with lithium upon discharge. During charging, two oxidation peaks rise at *ca.* 0.32 and 0.52 V (*vs.* Li/Li$^+$) for Li$_x$Si de-alloying. In the following cycles, the positions of oxidation and reduction peaks show a minimal shift, indicating good reversibility of Si@F–SiO$_x$/C-1. The intensities of these peaks continue to increase over successive cycles, attributed to the gradual activation of Si NPs encapsulated within the F–SiO$_x$/C sheath. Si@SiO$_x$/C exhibits a similar CV pattern to that of Si@F–SiO$_x$/C-1, showing that F-doping does not alter the electrochemical pathway of Si NPs for lithium storage (Fig. S6b, ESI†).

Lithium storage kinetics of Si@F–SiO$_x$/C-1 is analyzed by CV at various scan rates from 0.2 to 1.0 mV s$^{-1}$ (Fig. S7, ESI†). There is a relationship between the measured current ($i$) and scan rate ($\nu$): $i = a\nu^b$, where $a$ and $b$ are empirical constants, and $\nu$ represents the scan rate.[26] Ideally, a bulk diffusion-controlled process yields a $b$ value of 0.5, while a capacitive process induces a $b$ value of 1.0. The $b$ values of Si@F–SiO$_x$/C-1 and Si@SiO$_x$/C are 0.85 and 0.77, respectively (Fig. 3f). Apparently, lithium storage in both electrodes involves a combination of diffusion-controlled and pseudocapacitive processes. The diffusion-controlled process contributes to high capacity *via* a multiple-electron redox reaction, while the pseudocapacitive behavior ensures fast lithium storage *via* ionic adsorption and a redox reaction at the near electrode surface.[27] The contribution of both processes can be evaluated by the equation: $i(V) = a\nu^b = k_1\nu + k_2\nu^{1/2}$, where $k_1$, $k_2$, and $a$ are constants, and $i(V)$ represents the current at a specific voltage. The $k_1\nu$ and $k_2\nu^{1/2}$ reflect the contribution of capacitive and diffusion-controlled processes, respectively. The ratio of capacitive to diffusion-controlled contributions for lithium storage can be determined by the values of $k_1$ and $k_2$ at different voltages. For Si@F–SiO$_x$/C-1, the pseudocapacitive contribution exceeds 64% at a slow scan rate below 0.2 mV s$^{-1}$. As the scan rate increases from 0.4 to 1.0 mV s$^{-1}$, the capacitive

contribution rises from 71% to 79%, which is critical for achieving a high power rate at high current rates (Fig. 3g). High pseudocapacitive contribution of Si@F–SiO$_x$/C can be ascribed to: (i) efficient Li$^+$ adsorption facilitated by an amorphous F–SiO$_x$/C coating matrix enriched with surface-active sites and defects alongside improved conductivity and (ii) rapid redox reactions of Si NPs enabled by a reduced ion diffusion path and large surface-to-volume ratios. Si@SiO$_x$/C exhibits a similar trend, with a much lower capacitive contribution of 36–56% at the same scan rates (Fig. 3h). This explains the higher capacities of Si@SiO$_x$/C than that of Si@F–SiO$_x$/C-1 before 110 cycles.

After deep cycling, the Si@F–SiO$_x$ anode encounters a thickness increase of 44% and pronounced cracks as a result of significant Si volume expansion upon lithiation, causing rapid anode failure (Fig. 4a–c). In contrast, the Si@F–SiO$_x$/C-1 anode undergoes greatly reduced volume expansion of 18.2% without cracking after cycling (Fig. 4d–f). This finding highlights the critical role of F doping in reinforcing the coating sheath around Si NPs against volume change. To evaluate the impact of the F–SiO$_x$/C content on Si@F–SiO$_x$/C anode stability, two benchmark samples, Si@F–SiO$_x$/C-2 and Si@F–SiO$_x$/C-3, are prepared using a similar way to that of Si@F–SiO$_x$/C-1, except for reducing or increasing the organosilane amount, respectively. Among them, Si@F–SiOx/C-2 with the lowest SiO$_x$ content exhibits the highest capacities (750–920 mA h g$^{-1}$) at low current densities of 0.1–0.3 A g$^{-1}$ (Fig. S8, ESI†). However, it suffers rapid capacity decay at larger current densities due to insufficient buffering of Si volume expansion. Consequently, this anode exhibits a drastic thickness increase of 56.5% (Fig. S9, ESI†). The Si@F–SiO$_x$/C-3 anode with excess SiO$_x$ experiences a low expansion of 11.3% but delivers rather low capacities at various current densities. Apparently, optimizing the SiO$_x$ content is important to balance high capacities and robust stability for the Si@F–SiO$_x$/C anode.

Post-mortem XPS analysis of the cycled anode reveals that the presence of F species also facilitates the formation of an LiF-enriched
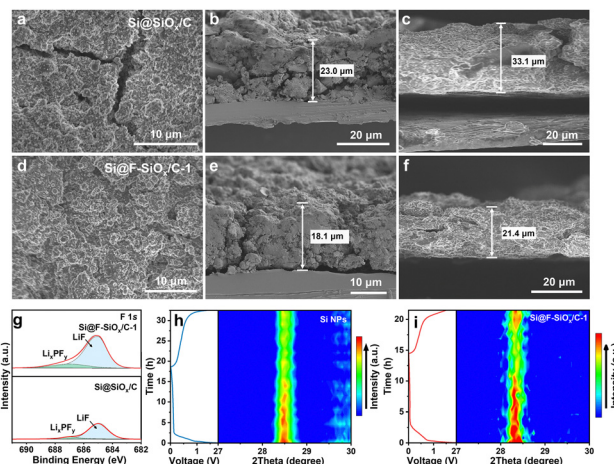
**Fig. 4** Top SEM views of (a) the Si@SiOₓ/C and (d) the Si@F–SiOₓ/C-1 anode after cycling. Cross-section SEM views of (b) and (c) Si@SiOₓ/C and (e) and (f) Si@F–SiOₓ/C-1 (b) and (e) before and (c) and (f) after cycling. (g) High-resolution F 1s XPS spectra of the SEI on Si@SiOₓ/C and Si@F–SiOₓ/C-1 after cycling. *In situ* XRD pattern of (h) Si@F–SiOₓ/C-1 and (i) bare Si NPs during a discharge–charge cycle.

SEI. In the C 1s spectra, the peaks at 290.7, 288.8, 286.7, and 284.8 eV correspond to $Li_2CO_3$ and organic species containing C=O, C–O and C–C bonds, respectively (Fig. S10, ESI†). The formation of LiF is identified by the peak at 55.8 eV in the Li 1s spectrum and the peaks at 685.0 eV in the F 1s XPS spectrum (Fig. 4g and Fig. S11, ESI†). Compared to Si@SiOₓ/C, a stronger signal of LiF from the SEI on the Si@F–SiOₓ/C-1 anode indicates the promoting effect of F doping on LiF-rich SEI formation. Coupled with flexible organic species, the high-modulus LiF-enriched SEI offers better accommodation of Si volume expansion, thereby enhancing cycling stability.[28] The beneficial effect of the F–SiOₓ/C coating on the structural stability of Si NPs is further confirmed by *in situ* XRD analysis. It reveals a gradual decline in the Si (111) peak during lithiation upon discharge, which recovers after delithiation during the subsequent charging for the Si@F–SiOₓ/C-1 anode (Fig. 4h). This observation indicates good reversibility of this anode for the transition between crystalline and amorphous states.[29] In contrast, the Si nanoparticle anode undergoes rapid and irreversible structural degradation, reflected by the rapid decay of the Si (111) peak throughout the discharge–charge cycle (Fig. 4i).

In summary, a fluorinated organosilane polycondensation strategy was proposed to coat an F-doped SiOₓ/C composite on Si NPs. Chemical bridging of silanol groups on the Si surface and hydroxyl groups of hydrolyzed organosilane enables the formation of a robust F-doped SiOₓ/C sheath on Si NPs. The combination of robust SiOₓ and conductive carbon enhances the structural integrity and conductivity of the coating sheath surrounding Si NPs. The F-doping facilitates the formation of a SiOₓ/C coating dominated by electrochemically less active $Si^{4+}$ species. Moreover, it also promotes the formation of a LiF-rich SEI, thereby strengthening the SEI and ionic transport during lithium storage. The synergistic effects of these components extend the lifetime of the Si@F–SiOₓ/C-1 anode to 500 cycles at a large current density of 1.0 A g$^{-1}$, achieving 87.5% capacity retention alongside elevated capacities and improved rate performance.

## Data availability

The data that support the findings of this study are available from the corresponding author upon reasonable request.

## Conflicts of interest

There are no conflicts to declare.

## Notes and references

1 W. J. Zhang, *J. Power Sources*, 2011, **196**, 13.
2 Y. An, Y. Tian, C. Liu, S. Xiong, J. Feng and Y. Qian, *ACS Nano*, 2022, **16**, 4560.
3 W. Cao, Q. Li, X. Yu and H. Li, *eScience*, 2022, **2**, 47.
4 A. L. Chen, N. Shang, Y. Ouyang, L. Mo, C. Zhou, W. W. Tjiu, F. Lai, Y. E. Miao and T. Liu, *eScience*, 2022, **2**, 192.
5 X. Zhao and V. P. Lehto, *Nanotechnology*, 2021, **32**, 042002.
6 H. Wu and Y. Cui, *Nano Today*, 2012, **7**, 414.
7 H. Su, X. Li, C. Liu, Y. Shang and H. Liu, *Chem. Eng. J.*, 2023, **451**, 138394.
8 W. An, B. Gao, S. Mei, B. Xiang, J. Fu, L. Wang, Q. Zhang, P. K. Chu and K. Huo, *Nat. Commun.*, 2019, **10**, 1447.
9 H. Zhao, K. Liang, S. Wang, Z. Ding, X. Huang, W. Chen, Y. Ren and J. Li, *Adv. Sci.*, 2023, **10**, 2303696.
10 H. Zhang, R. Hu, S. Feng, Z. Lin and M. Zhu, *eScience*, 2023, **3**, 100080.
11 F. Wang, Y. Wang, Z. Liu, C. Zhang, L. Li, C. Ye, J. Liu and J. Tan, *Adv. Energy Mater.*, 2023, **13**, 2301456.
12 S. Chen, Z. Song, L. Wang, H. Chen, S. Zhang, F. Pan and L. Yang, *Acc. Chem. Res.*, 2022, **55**, 2088.
13 P. Xiao, X. Yun, Y. Chen, X. Guo, P. Gao, G. Zhou and C. Zheng, *Chem. Soc. Rev.*, 2023, **52**, 5255.
14 J. Chen, X. Fan, Q. Li, H. Yang, M. R. Khoshi, Y. Xu, S. Hwang, L. Chen, X. Ji, C. Yang, H. He, C. Wang, E. Garfunkel, D. Su, O. Borodin and C. Wang, *Nat. Energy*, 2020, **5**, 386.
15 G. Hu, R. Yu, Z. Liu, Q. Yu, Y. Zhang, Q. Chen, J. Wu, L. Zhou and L. Mai, *ACS Appl. Mater. Interfaces*, 2021, **13**, 3991.
16 R. Gogoi and A. K. Tyagi, *J. Nat. Fibers*, 2021, **18**, 803.
17 J. Ge, H. Shen, F. Zhou, Y. Li, N. Yuan, W. Yang, H. Zhou, B. Xu, R. Guo and P. Xu, *J. Mater. Chem. A*, 2022, **10**, 1928.
18 R. Wang, J. Wang, S. Chen, W. Bao, D. Li, X. Zhang, Q. Liu, T. Song, Y. Su and G. Tan, *ACS Appl. Mater. Interfaces*, 2021, **13**, 5008.
19 A. B. M. Giasuddin, A. Cartwright and D. W. Britt, *ACS Appl. Nano Mater.*, 2021, **4**, 4092.
20 H. Yen, S. Jou and C. J. Chu, *Mater. Sci. Eng., B*, 2005, **122**, 240.
21 R. Yu, Y. Pan, Y. Jiang, L. Zhou, D. Zhao, G. Van Tendeloo, J. Wu and L. Mai, *Adv. Mater.*, 2023, **35**, 2306504.
22 B. J. Jang, Q. Zhao, J. H. Baek, J. M. Seo, J. P. Jeon, D. H. Kweon, G. F. Han, C. Xu and J. B. Baek, *Adv. Funct. Mater.*, 2023, **33**, 2306426.
23 Y. Chen, Y. Lin, N. Du, Y. Zhang, H. Zhang and D. Yang, *Chem. Commun.*, 2017, **53**, 6101.
24 K. Kitada, O. Pecher, P. C. M. M. Magusin, M. F. Groh, R. S. Weatherup and C. P. Grey, *J. Am. Chem. Soc.*, 2019, **141**, 7014.
25 S. Sim, P. Oh, S. Park and J. Cho, *Adv. Mater.*, 2013, **25**, 4498.
26 V. Augustyn, P. Simon and B. Dunn, *Energy Environ. Sci.*, 2014, **7**, 1597.
27 S. Niu, Z. Wang, M. Yu, M. Yu, L. Xiu, S. Wang, X. Wu and J. Qiu, *ACS Nano*, 2018, **12**, 3928.
28 W. Huang, Y. Wang, L. Lv, G. Zhu, Q. Qu and H. Zheng, *Energy Storage Mater.*, 2023, **60**, 102837.
29 X. Xue, B. Lou, C. Wu, W. Pang, J. Zhang, N. Shi, Z. Men, F. Wen, X. Yang, J. Wu, L. Tian and D. Liu, *Chem. Eng. J.*, 2024, **488**, 150936.